Shock leakage through an unsteady vortex-laden mixing layer: application to jet screech

By TAKAO SUZUKI† AND SANJIVA K. LELE

Department of Aeronautics and Astronautics, Stanford University, Stanford, CA 94305, USA

In an under-expanded supersonic jet, the interaction between shock-cell structure and vortices in a mixing layer generates intense tonal noise, called jet screech. This noise generation can be explained as a shock-leakage process through an unsteady vortex-laden mixing layer. This paper studies the shock-leakage mechanism based on a geometrical theory and direct numerical simulation (DNS) in two dimensions. In the limit of weak shocks, the analysis becomes analogous to geometrical acoustics: the eikonal equation demonstrates that shock waves tend to leak near the saddle points between vortices. Analysing the wavenumber vector, it is shown that the local vorticity behaves as a barrier against shocks. Using the unsteady DNS data, trajectories of the shock fronts are computed with the time dependent eikonal equation. Furthermore, the interaction between unsteady vortices and a compression wave is solved using DNS. The geometrical theory shows good agreement with DNS for shock-front evolution, but the amplitude of the leaked waves agrees only qualitatively. This study also investigates the effects of a temperature difference across the mixing layer. The analysis based on total internal reflection and the numerical results of both geometrical acoustics and DNS indicate that the direction of the radiated shock noise tends to rotate downstream as the jet temperature increases.

1. Introduction

When a supersonic jet is under-expanded, the pressure mismatch generates a shock-cell pattern, which must be confined to the core region if the jet flow is perfectly steady. The angle of weak shock cells is nearly aligned with the Mach angle, and this angle exceeds the 'critical angle' beyond which total internal reflection occurs. Therefore, no acoustic waves associated with the shock should propagate across the mixing layer. However, flow instability invokes large-scale vortices in the mixing layer, and these disturbances interact with the shock-cell structure. As a result, some acoustic energy associated with the shock can propagate across the mixing layer and, in turn, radiate as a discrete tone in the far field (see figure 1). This acoustic radiation, referred to as shock noise, propagates even upstream and excites new instability waves from the nozzle lip. Thus, the whole system composes a feedback loop resulting in large resonant amplification of discrete tones. In fact, this phenomenon, called 'jet screech', has been investigated in many experimental studies (Krothapalli *et al.* 1986; Walker & Thomas 1997; Panda 1998, 1999; and Raman 1999 for a recent review), and the frequency of the tone has been successfully predicted (Powell 1953; Tam, Seiner &

† Present address: California Institute of Technology, Division of Engineering and Applied Science, Pasadena, CA 91125, USA.
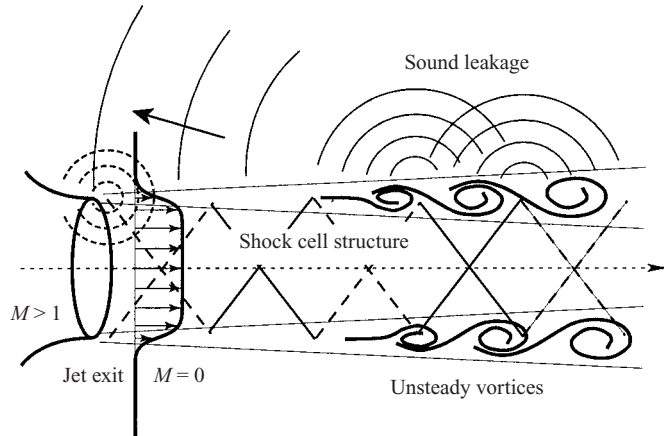
FIGURE 1. Diagram of jet screech.

Yu 1986; Tam 1988; Norum 1991); however, its intense sound generation mechanism still remains somewhat elusive.

To explain the tonal noise generation mechanism, several studies (Howe & Ffowcs Williams 1978; Tam & Tanna 1982; Kerschen & Cain 1995) have modelled it as nonlinear interaction between the shock-cell structure and shear-layer instability waves. Although these studies explained weak sound emission, they were not able to explain the intense noise generation. Furthermore, success in a theoretical prediction of the waveform of shock noise as well as its amplitude has been limited. A recent work (Manning & Lele 2000) introduced geometrical acoustics to explain the sound radiation pattern of shock noise. In fact, their computational results successfully visualized the shock-leakage phenomenon, and the comparison between the linearized Euler equations and the numerical computation of the eikonal equation using the Stuart vortex model (Stuart 1967) showed good agreement. However, the validity of the high-frequency limit for standing shock waves was uncertain, and the amplitude was still unpredictable.

The objective of this paper is to identify the mechanism for intense sound generation of shock noise and to predict its amplitude as well as the wavefront evolution. The key idea exploited here is the coincidence between the ray trajectory and the shock-front, in other words, the similarity between geometrical acoustics and shock deformation. Making use of the similarity, this study investigates the condition for shock leakage, especially focusing on the effects of the temperature ratio across the mixing layer. Furthermore, this paper studies a method to predict the amplitude of shock noise using a geometrical theory.

In the past, the interaction of a shock wave and weak vortical disturbances has been extensively investigated (Moore 1953; Ribner 1954; and others). These studies have shown that vortical disturbances distort shock-fronts. A method of this type, so-called 'linear interaction analysis', assumes small amplitude in base flow disturbances although the nonlinear jump condition across the shock is taken into account. On the other hand, weak shock motions with an arbitrary base flow have been also investigated. Keller (1954) initially developed the theory, and Whitham (1974) extended this type of analysis for nonlinear shocks. Several studies (Kevlahan 1996; Monica & Prasad 2001) have computationally investigated these methods;

in particular, Kevlahan (1996) studied the interaction between a shock and a two-dimensional vortex array. However, most of these works have focused on steady base flows. The present work solves unsteady shock motions with a large-scale unsteady base flow by simplifying the jump condition as isentropic and developing the equations in space–time coordinates.

The main point of the theoretical development is as follows: a line of discontinuity corresponding to the wavefront of a compression wave or a weak shock can be solved using the eikonal equation (the ray-tracing equation). Likewise, the strength of the discontinuity can be given by the solution to the transport equation. The key is to replace the phase part of geometrical expansion ($\exp(i\omega\phi)$) by a sharp ramp function (such as, $\tanh(\phi/\epsilon)$) and to replace the amplitude part by the strength of discontinuity. Consequently, the high-frequency limit ($\omega \to \infty$) becomes analogous to the steep limit of the ramp function ($\epsilon \to 0$). Namely, the governing equation derived based on geometrical acoustics is identical to the convective wave equation for the evolution of discontinuity.

This analogy gives the condition for intense shock noise generation due to large-scale disturbances. If a ray initially aligned with the Mach angle penetrates the mixing layer, small portions of the shock radiate to the far field as sound waves. The system of the eikonal equation shows that the velocity gradient tensor characterizes the evolution of wavefronts, and the decomposition of the velocity gradient tensor implies that vorticity distribution behaves as a barrier against shocks. Therefore, shocks tend to leak from regions in which the local vorticity becomes weak, i.e. near the saddle points. In addition, the effects of the temperature ratio are analysed by comparing the Mach angle and the critical angle of total internal reflection.

The theoretical analyses are verified by performing direct numerical simulation (DNS) and also by numerically solving the time-dependent eikonal equation. As a model problem, a supersonic mixing layer ($M_1 = 1.2$) is computed using the full Navier–Stokes equations in two dimensions, in which the interaction between the compression wave and the unsteady vortex-laden mixing layer is directly solved. Making use of the unsteady direct numerical simulation (DNS) data, trajectories of shock-fronts are calculated based on the time-dependent eikonal equation. The time evolution of compression and expansion wavefronts obtained from DNS is compared with that solved using the eikonal equation; similarly, the amplitude measured from DNS is compared with that using the transport equation to study the directivity. The comparison of the wavefront shows fairly good agreement although the amplitude agrees only qualitatively.

To investigate the temperature dependence, three cases are simulated with the temperature ratio of the ambient to the jet being $T_1/T_2 = 0.75$, 1.0 and 1.5 at the free-stream Mach number of $M_1 = 1.2$. The DNS results indicate that as the jet temperature increases, the radiated shock noise tends to lean toward downstream when the pressure disturbance levels of instability waves are equal. This tendency can be deduced from the analysis based on total internal reflection in a steady mixing layer.

The outline of this paper is as follows. The theoretical background is described in §2. The governing equations for the evolution of weak shocks are developed using the similarity between geometrical acoustics and shock deformation. The dependence on the temperature ratio is analysed based on total internal reflection in a steady mixing layer. The mechanism of the sound leakage is explained based on the eikonal equation. In §3, the numerical procedures of DNS and time-dependent geometrical acoustics are described. In §4, the numerical results are discussed. This includes

extensive comparisons with the geometrical theory, which verify the sound-leakage mechanism discussed in §2. Conclusions are presented in the last section.

2. Theoretical approach

2.1. *Similarity between shock deformation and geometrical acoustics*

To study the shock–vortex interaction in the context of jet screech, Manning & Lele (2000) introduced geometrical acoustics and numerically demonstrated that the solution obtained from geometrical acoustics coincides with the wavefront of shock noise; however, the validity of the high-frequency limit applying to standing shock waves was uncertain. This section gives a formal derivation of a method to estimate the sound pressure level of shock waves using the similarity between the deformation of weak shocks and geometrical acoustics. Analyses similar to this type in different contexts may be seen in Keller (1954), Whitham (1974), Kevlahan (1996), Monica & Prasad (2001), and others. The method described here is applicable to unsteady base flows in arbitrary dimensions.

Consider a slightly under-expanded jet in which a standing shock wave is distorted by large-scale vortices in the mixing layer. The strength of the shock is assumed small ($\Delta p/p_\infty \ll 1$, p_∞ being the ambient pressure) so that the flow is isentropic and the shock does not disturb the base flow. Therefore, the steady deflection downstream of the interaction defined by $\theta_d \equiv (2\sqrt{M_1^2 - 1}/\gamma M_1^2)(\Delta p/p_\infty)$, where γ is the specific heat ratio and M_1 the jet Mach number (cf. Kerschen & Cain 1995), is ignored in later analysis. Now, the pressure field is solved as a solution to the acoustic mode in a shear flow. For a transversely sheared base flow the third-order convective wave equation, referred to as the Pridmore-Brown equation (Pridmore-Brown 1958) or Lilley's equation (Lilley 1974), is expected to represent the solution:

$$\frac{\mathrm{D}}{\mathrm{D}t}\left[\frac{\mathrm{D}^2\Pi}{\mathrm{D}t^2} - \frac{\partial}{\partial x_j}\left(a^2\frac{\partial\Pi}{\partial x_j}\right)\right] + 2\frac{\partial u_k}{\partial x_j}\frac{\partial}{\partial x_k}\left(a^2\frac{\partial\Pi}{\partial x_j}\right) = -2\frac{\partial u_i}{\partial x_j}\frac{\partial u_j}{\partial x_k}\frac{\partial u_k}{\partial x_i}, \qquad (2.1)$$

where, $\mathrm{D}/\mathrm{D}t \equiv \partial/\partial t + u_j\partial/\partial x_j$, and $\Pi \equiv \gamma^{-1}\log(p/p_\infty)$. It should be emphasized that each quantity includes three parts, the mean, the unsteady vortical disturbance, and the acoustic disturbance (i.e. $p = p_\infty + p^{vor} + p^{ac}$, etc.), where the magnitude of the acoustic disturbance is much smaller than the other two parts. To non-dimensionalize the equation, the following characteristic scales are used: the speed of sound inside the jet a_j is taken to be the velocity scale, and the vorticity thickness δ_V to be the length scale. Therefore, u_i denotes the local Mach number multiplied by the local speed of sound, and a^2 denotes the local temperature assuming an ideal gas law.

When the acoustic wavelength is much shorter than the length scale over which the medium varies (the vorticity thickness in the present case), and also the acoustic frequency is much higher than the inverse time scale of medium evolution, we can assume a high-frequency limit and apply geometrical acoustics. In such a case, we should express the acoustic pressure disturbance by

$$\Pi^{ac}(t, \boldsymbol{x}) \equiv \frac{1}{\gamma}\frac{p^{ac}}{p} = \frac{1}{\gamma}\frac{P(t, \boldsymbol{x})}{p}\exp[\mathrm{i}\omega\phi(t, \boldsymbol{x})] \equiv P^\bullet(t, \boldsymbol{x})\exp[\mathrm{i}\omega\phi(t, \boldsymbol{x})], \qquad (2.2)$$

where $P^\bullet \equiv P/(\gamma p)$. Velocity and temperature associated with the acoustic disturbance can be similarly expanded. Likewise, consider a compression wave whose pressure

amplitude is sufficiently weak but which is extremely narrow:

$$\Pi^{comp}(t, \boldsymbol{x}) \equiv P^\bullet(t, \boldsymbol{x}) h[\phi(t, \boldsymbol{x})/\epsilon], \tag{2.3}$$

where $P^\bullet(t, \boldsymbol{x}) \equiv P(t, \boldsymbol{x})/(\gamma p)$ ($|P| \ll 1$), P corresponding to the strength of the compression wave in terms of pressure and ϵ ($0 < \epsilon \ll 1$) to the width of the compression wave, and suppose that $|\partial P^\bullet/\partial t|$, $|\partial P^\bullet/\partial x_i| \ll \epsilon^{-1}$. Here, $h[z]$ is a monotonically increasing function satisfying $h[-\infty] = 0$ and $h[+\infty] = 1$. For example, Taylor's weak shock profile (Lighthill 1956) yields $h[x/\epsilon] = [1 + \tanh(x/\epsilon)]/2$ where $\epsilon \equiv 4/(\gamma + 1)(4/3 + (\gamma - 1)/Pr)\mu a/\Delta p$ (Pr being the Prandtl number and μ the viscosity). Accordingly, $h[z]$ has the following character:

$$\lim_{\epsilon \to 0} h[\phi/\epsilon] = H(\phi) \equiv \begin{cases} 0 & \text{if } \phi < 0, \\ 1 & \text{if } \phi \geqslant 0. \end{cases} \tag{2.4}$$

Therefore, the limit of $\epsilon \to 0$ corresponds to a weak shock wave, and a curve satisfying $\phi(t, \boldsymbol{x}) = 0$ represents its wavefront. Again, the term 'weak' indicates that the flow is still considered to be isentropic across the shock.

Now, compare (2.2) and (2.3), and observe their similarity. In the case of geometrical acoustics, (2.2) and the corresponding acoustic velocity and temperature disturbances are substituted into (2.1), and they are asymptotically expanded for large ω. By taking the leading terms of ω, the eikonal equation is obtained:

$$(\phi_t + u_j \phi_j)^2 - a^2 \phi_j^2 = 0, \tag{2.5}$$

where $\phi_t \equiv \partial \phi/\partial t$, which corresponds to the local frequency, and $\phi_i \equiv \partial \phi/\partial x_i$ to the local wavenumber vector. Likewise, in case of a weak shock or a compression wave, take the leading terms for small ϵ; as a result, the same eikonal equation is obtained. Now, $(\phi_t, \boldsymbol{\phi}_i)$ represents the direction normal to the shock-front in space–time coordinates.

To solve for the shock-front, we can apply the method of characteristics, i.e. break the eikonal equation (2.5) into the following ODE system:

$$\frac{\mathrm{d}t}{\mathrm{d}\tau} = 1, \tag{2.6}$$

$$\frac{\mathrm{d}x_i}{\mathrm{d}\tau} = -\frac{a^2}{\phi_t + u_k \phi_k}\phi_i + u_i, \tag{2.7}$$

$$\frac{\mathrm{d}\phi_t}{\mathrm{d}\tau} = -\frac{\partial u_k}{\partial t}\phi_k + \frac{\phi_t + u_k \phi_k}{2a^2}\frac{\partial a^2}{\partial t}, \tag{2.8}$$

$$\frac{\mathrm{d}\phi_i}{\mathrm{d}\tau} = -\frac{\partial u_k}{\partial x_i}\phi_k + \frac{\phi_t + u_k \phi_k}{2a^2}\frac{\partial a^2}{\partial x_i}, \tag{2.9}$$

$$\frac{\mathrm{d}\phi}{\mathrm{d}\tau} = 0. \tag{2.10}$$

Equation (2.10) shows that characteristic curves are iso-contours of ϕ, one of which is equivalent to the shock-front, say $\phi = 0$. In this system, the parameterization of the curve, τ, is normalized so that it is identical to the time scale. Thus, imposing the initial conditions corresponding to a standing shock in the free-stream region, the shock-front can be followed over the course of time. Note that this equation system (2.6)–(2.10) is integrated in space–time coordinates; therefore, the instantaneous shock-front is a cut of a characteristic bundle at constant time, not a projection of a characteristic curve.

Next, to solve for the amplitude fields, derive the first-order transport equation. Substituting (2.3) and the corresponding acoustic velocity and temperature disturbances into (2.1), we can follow the method used in geometrical acoustics. Taking the second highest order of ϵ^{-1}, it yields

$$
2(P_t^\bullet + u_j P_j^\bullet)(\phi_t + u_k \phi_k) - 2a^2 P_j^\bullet \phi_j + \frac{2a^2 P^\bullet \phi_j \phi_k}{\phi_t + u_l \phi_l} \frac{\partial u_k}{\partial x_j}
$$
$$
+ P^\bullet \left[3 \left(\phi_{tt} + 2u_j \phi_{tj} + u_j u_k \phi_{jk} + \phi_j \frac{\mathrm{D} u_j}{\mathrm{D} t} \right) - a^2 \phi_{jj} \right]
$$
$$
- P^\bullet \left[\gamma \phi_j \frac{\partial p}{\partial x_j} + \phi_j \frac{\partial a^2}{\partial x_j} + \frac{\phi_j^2}{\phi_t + u_l \phi_l} \frac{\mathrm{D} a^2}{\mathrm{D} t} + \frac{2a^2 \phi_j (\phi_{tj} + u_k \phi_{jk})}{\phi_t + u_l \phi_l} \right] = 0. \quad (2.11)
$$

Here, again $P_t^\bullet \equiv \partial P^\bullet / \partial t$ and $P_i^\bullet \equiv \partial P^\bullet / \partial x_i$. To simplify (2.11), note that the differentiation of (2.5) by $\mathrm{D}/\mathrm{D}t$ gives

$$
2 \left(\phi_{tt} + 2u_j \phi_{tj} + u_j u_k \phi_{jk} + \phi_j \frac{\mathrm{D} u_j}{\mathrm{D} t} \right) + \frac{2a^2 \phi_j \phi_k}{\phi_t + u_l \phi_l} \frac{\partial u_k}{\partial x_j}
$$
$$
- \left[\phi_j \frac{\partial a^2}{\partial x_j} + \frac{\phi_j^2}{\phi_t + u_l \phi_l} \frac{\mathrm{D} a^2}{\mathrm{D} t} + \frac{2a^4 \phi_j \phi_k \phi_{jk}}{(\phi_t + u_l \phi_l)^2} \right] = 0. \quad (2.12)
$$

Using these relations, substitute (2.12) into (2.11). After simplifying it with (2.6) and (2.7), we can obtain the following conservation form:

$$
\frac{\partial}{\partial t} \left[\frac{(P^\bullet)^2 p}{\phi_t + u_k \phi_k} \frac{\mathrm{d} t}{\mathrm{d} \tau} \right] + \frac{\partial}{\partial x_j} \left[\frac{(P^\bullet)^2 p}{\phi_t + u_k \phi_k} \frac{\mathrm{d} x_j}{\mathrm{d} \tau} \right] = 0. \quad (2.13)
$$

Hence, the quantity

$$
\frac{P^2 S}{p(\phi_t + u_k \phi_k)} \sqrt{a_\infty^2 \left| \frac{\mathrm{d} t}{\mathrm{d} \tau} \right|^2 + \left| \frac{\mathrm{d} \boldsymbol{x}}{\mathrm{d} \tau} \right|^2} = \text{Const.} \quad (2.14)
$$

is conserved along 'tubes' consisting of characteristic bundles in a four-dimensional sense (see figure 2). Here, S denotes the area of the tube normal to the direction of characteristic lines in four dimensions (here, the time coordinate is normalized using the ambient speed of sound): $(a_\infty \mathrm{d} t / \mathrm{d} \tau, \mathrm{d} \boldsymbol{x} / \mathrm{d} \tau)$. This quantity (2.14) is analogous to the 'Blokhintzev invariant' (Blokhintzev 1946) of geometrical acoustics. Therefore, the field of $P(t, \boldsymbol{x})$ is the same as the amplitude field of sound waves whose incident propagation direction is aligned with the Mach angle. In numerical simulations, the variation of S can be computed by issuing two families of such incident rays separated by a small distance, say Δw, and by keeping track of this distance and the ray direction.

To solve the ODE system (2.6)–(2.10), set the initial conditions as follows so that they satisfy the eikonal equation (2.5):

$$
x(0) = x_s, \quad (2.15)
$$
$$
y(0) = y_s, \quad (2.16)
$$
$$
\phi_t(0) = 0, \quad (2.17)
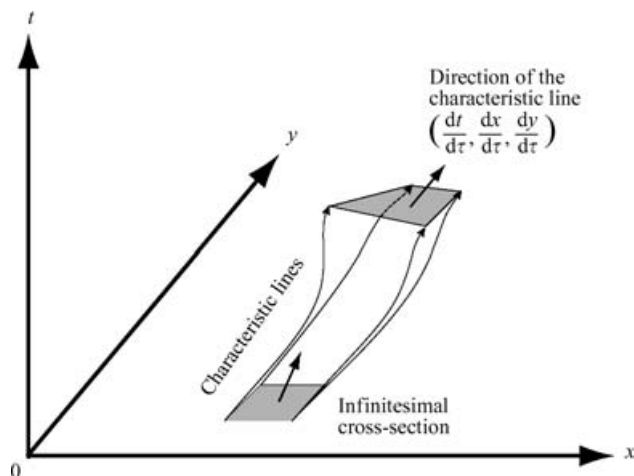$$
$$
\phi_x(0) = -\frac{1}{a_s M_s}, \quad (2.18)
$$

FIGURE 2. Diagram of a ray tube or a 'characteristic bundle' for the time-dependent geometrical acoustics.

$$\phi_y(0) = \frac{1}{a_s}\sqrt{1 - \frac{1}{M_s^2}}, \tag{2.19}$$

$$\phi(0) = 0, \tag{2.20}$$

where quantities with the subscript '*s*' are evaluated at the initial position (x_s, y_s) which is located on the shock-front in the free stream. Here, the initial direction of characteristic curves is given by $\tan\theta_s = 1/\sqrt{M_s^2 - 1}$, which is identical to the Mach angle. With these initial conditions, the time-dependent ODE system (2.6)–(2.10) can be integrated together with the unsteady base flow data.

2.2. *Analysis based on the total internal reflection*

The condition for shock leakage across a vortex-laden mixing layer is one of the main interests. As mentioned before, such a condition can be analysed using the analogy between a ray trajectory and a shock-front. In the case of a ray trajectory, if the mixing layer is steady and the angle of incidence in the free stream exceeds the 'critical angle', no ray can penetrate the mixing layer, referred to as 'total internal reflection' (see figure 3*a*). Since the Mach angle is always greater than the critical angle, the shocks are confined to the core region forming a shock-cell pattern in a steady flow. However, in an unsteady mixing layer, vortical disturbances allow some portions of the shock to leak across the mixing layer and to radiate as sound waves (figure 3*b*). As the critical angle is a function of the free-stream Mach number and the temperature ratio, we could postulate that the shock-leakage condition follows the difference between the critical angle and the Mach angle.

To derive the condition for total internal reflection, consider a transversely sheared mixing layer in two dimensions. Similar types of analyses regarding total internal reflection can be found in various contexts, such as Goldstein (1976). Now, suppose that the free-stream Mach number on the lower side is supersonic ($M_1 > 1$), and the upper side is quiescent ($M_2 = 0$). Figure 4 depicts a schematic of the flow geometry. Here, the subscripts 1 and 2 denote the lower and upper sides, respectively. Likewise, the speed of sound on the lower side is $a_1 = a_j \equiv 1$, and that on the upper side is a_2. Consider plane waves incident from the lower side and refracted in the mixing
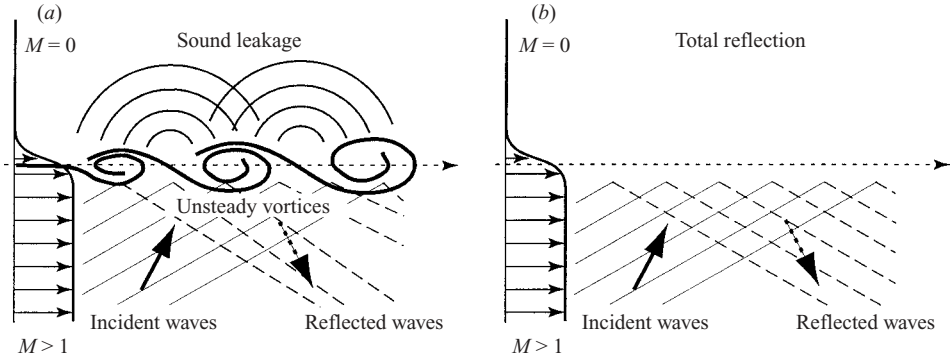
FIGURE 3. Plane wave propagation across a two-dimensional mixing layer.
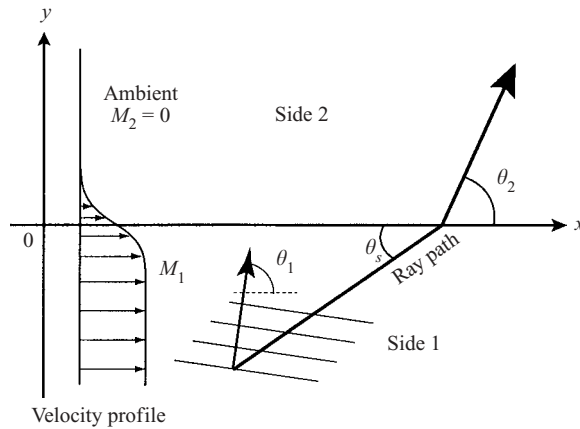(*a*) Steady mixing layer. (*b*) Unsteady mixing layer.

FIGURE 4. Flow geometry and coordinate system.

layer. Knowing that $\partial u_k / \partial x_j$ for the base flow vanishes in the free stream, the form of the plane wave solution, $\Pi \sim \exp[-i\omega(t - \bar{k}_x x - \bar{k}_y y)]$, is substituted into (2.1). Consequently, the solution for the wavenumber in the flow direction can be obtained as follows:

$$\bar{k}_x = \frac{\cos\theta_1}{a_1(1 + M_1 \cos\theta_1)} \quad \text{at} \quad y = -\infty, \qquad (2.21)$$

$$\bar{k}_x = \frac{\cos\theta_2}{a_2} \quad \text{at} \quad y = +\infty. \qquad (2.22)$$

Here, $M_1 \equiv u_1/a_1 \; (= u_1)$, and θ denotes the angle normal to the wavefront. (Note θ_1 is not identical to the ray direction on the lower side. See figure 4 again.) As the flow is homogeneous in the x-direction, $\bar{k}_x$ is independent of the velocity and temperature profiles in the mixing layer. Therefore, if $|\cos\theta_2| = |a_2\bar{k}_x| > 1$, no incident waves propagate on the upper side. This yields the condition for total internal reflection,

$$\theta_1 < \theta_1^{cr} \equiv \arccos\left(\frac{-1}{a_2/a_1 + M_1}\right). \qquad (2.23)$$

Figure 5 plots the critical angle θ_1^{cr} as a function of the Mach number and compares it with the Mach angle, defined by $\theta_1^M \equiv \arccos(-1/M_1)$. It shows that θ_1^{cr} increases in
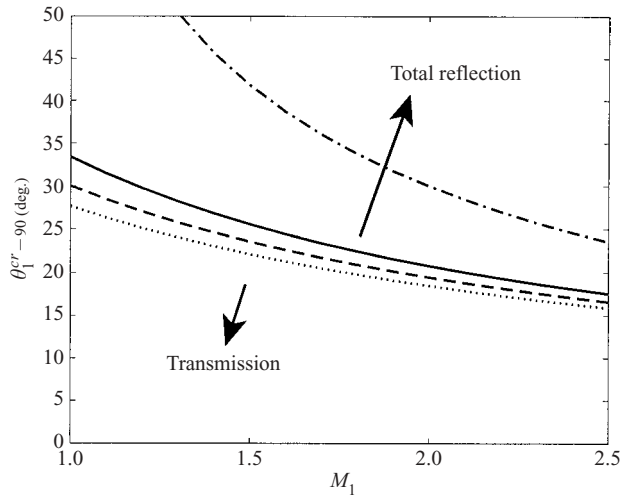
FIGURE 5. Mach angle and critical angle for total internal reflection: $- \cdot -$, Mach angle; $\cdots$, critical angle of cold jet ($T_1/T_2 = 0.75$); $---$, iso-thermal jet ($T_1/T_2 = 1.$); ———, hot jet ($T_1/T_2 = 1.5$).

a hot jet ($a_2/a_1 < 1$) and comes closer to the Mach angle, while θ_1^{cr} decreases in a cold jet ($a_2/a_1 > 1$) provided that the Mach number is fixed. This suggests a hypothesis that as the jet temperature increases, weak shocks can more easily penetrate the mixing layer and propagate more toward downstream. This hypothesis is examined using numerical simulations in §4.1.

2.3. *Mechanism of intense shock noise generation*

As (2.23) shows, the critical angle is always lower than the Mach angle; hence, shock leakage never occurs in a steady jet mixing layer. Therefore, intense shock noise generation requires unsteady disturbances. In this paper the term 'steady' refers to the case in which the mixing layer is undisturbed (as described in the previous section), while the term 'unsteady' refers to the case in which the mixing layer includes large-scale disturbances, namely a 'vortex-laden' mixing layer. However, the analysis for the 'unsteady' case in this section is carried out in the frame moving with the convective velocity of the disturbance, and the base flow field is assumed steady. Nonetheless, the word 'unsteady' is used for convenience. In this section, the sound-leakage mechanism is analysed in an 'unsteady' mixing layer based on the eikonal equation.

In two dimensions, the time-evolution of the direction normal to the wavefront, (2.8) and (2.9), can be rewritten as the following linear system:

$$\frac{\mathrm{d}}{\mathrm{d}t} \begin{pmatrix} \phi_t \\ \phi_x \\ \phi_y \end{pmatrix} = \begin{pmatrix} \dfrac{1}{2a^2}\dfrac{\partial a^2}{\partial t} & -\dfrac{\partial u}{\partial t} + \dfrac{u}{2a^2}\dfrac{\partial a^2}{\partial t} & -\dfrac{\partial v}{\partial t} + \dfrac{v}{2a^2}\dfrac{\partial a^2}{\partial t} \\ \dfrac{1}{2a^2}\dfrac{\partial a^2}{\partial x} & -\dfrac{\partial u}{\partial x} + \dfrac{u}{2a^2}\dfrac{\partial a^2}{\partial x} & -\dfrac{\partial v}{\partial x} + \dfrac{v}{2a^2}\dfrac{\partial a^2}{\partial x} \\ \dfrac{1}{2a^2}\dfrac{\partial a^2}{\partial y} & -\dfrac{\partial u}{\partial y} + \dfrac{u}{2a^2}\dfrac{\partial a^2}{\partial y} & -\dfrac{\partial v}{\partial y} + \dfrac{v}{2a^2}\dfrac{\partial a^2}{\partial y} \end{pmatrix} \begin{pmatrix} \phi_t \\ \phi_x \\ \phi_y \end{pmatrix}, \quad (2.24)$$

where the velocity components are rewritten as $u \equiv u_1$ and $v \equiv u_2$.

To observe the overall sound-leakage mechanism, consider (2.24) in a frame moving with the convective velocity of the vortices, u_c, where the subscript c denotes the

convective frame. In this frame, the time scale of the motions associated with instability waves is given by $1/(u_c \times \mathrm{Im}[k_x^{IN}])$, where k_x^{IN} denotes the complex wavenumber of the instability waves in the x-direction. When this time scale is much longer than the acoustic time scale associated with the spatial variation of the medium, i.e. δ_V/a, the unsteady terms can be ignored (i.e. frozen flow). In other words, $|(1/a)(\partial/\partial t)| \sim |M_c \times \mathrm{Im}[k_x^{IN}]| \ll 1/\delta_V \sim |\partial/\partial x_i|$, where M_c denotes the convective Mach number of the vortices. In such a frame, (2.24) can be approximated as

$$
\frac{\mathrm{d}}{\mathrm{d}t}\begin{pmatrix}\phi_x\\\phi_y\end{pmatrix}=\left[\begin{pmatrix}-\dfrac{\partial u}{\partial x}&-\dfrac{\partial v}{\partial x}\\[2mm]-\dfrac{\partial u}{\partial y}&-\dfrac{\partial v}{\partial y}\end{pmatrix}+\begin{pmatrix}\dfrac{u}{2a^2}\dfrac{\partial a^2}{\partial x}&\dfrac{v}{2a^2}\dfrac{\partial a^2}{\partial x}\\[2mm]\dfrac{u}{2a^2}\dfrac{\partial a^2}{\partial y}&\dfrac{v}{2a^2}\dfrac{\partial a^2}{\partial y}\end{pmatrix}\right]\begin{pmatrix}\phi_x\\\phi_y\end{pmatrix}-\begin{pmatrix}\dfrac{1}{2a^2}\dfrac{\partial a^2}{\partial x}\\[2mm]\dfrac{1}{2a^2}\dfrac{\partial a^2}{\partial y}\end{pmatrix},
$$

(2.25)

where u in the original frame is replaced by $u - u_c$. It is important to note that the solution to the eikonal equation in terms of the wavenumber vector is invariant to the choice of references. Defining

$$
A_v(t, x(t), y(t)) \equiv \begin{pmatrix}-\dfrac{\partial u}{\partial x}&-\dfrac{\partial v}{\partial x}\\[2mm]-\dfrac{\partial u}{\partial y}&-\dfrac{\partial v}{\partial y}\end{pmatrix},
$$

$$
A_t(t, x(t), y(t)) \equiv \begin{pmatrix}\dfrac{u}{2a^2}\dfrac{\partial a^2}{\partial x}&\dfrac{v}{2a^2}\dfrac{\partial a^2}{\partial x}\\[2mm]\dfrac{u}{2a^2}\dfrac{\partial a^2}{\partial y}&\dfrac{v}{2a^2}\dfrac{\partial a^2}{\partial y}\end{pmatrix},
$$

and

$$
B(t, x(t), y(t)) \equiv -\begin{pmatrix}\dfrac{1}{2a^2}\dfrac{\partial a^2}{\partial x}\\[2mm]\dfrac{1}{2a^2}\dfrac{\partial a^2}{\partial y}\end{pmatrix},
$$

(2.25) can be expressed as

$$
\frac{\mathrm{d}}{\mathrm{d}t}\begin{pmatrix}\phi_x\\\phi_y\end{pmatrix}=(A_v+A_t)\begin{pmatrix}\phi_x\\\phi_y\end{pmatrix}+B.
$$

(2.26)

For simplicity, first, consider the special case of an isothermal flow; thus, only the velocity gradient tensor A_v remains, and it may be decomposed into three parts:

$$
\begin{aligned}
A_v &= \tfrac{1}{2}(\lambda_1+\lambda_2)I+\tfrac{1}{2}\left[(A_v+A_v^T)-(\lambda_1+\lambda_2)I\right]+\tfrac{1}{2}\left(A_v-A_v^T\right)\\
&\equiv \quad\quad D_v \quad+\quad\quad\quad\quad S_v \quad\quad\quad\quad\quad\quad+\quad R_v,
\end{aligned}
$$

(2.27)

where λ_1 and λ_2 denote the eigenvalues of A_v, and D_v represents dilatation, S_v shear-strain, and R_v rotation. In particular, the rotation part can be expressed in terms of the local vorticity ω:

$$
R_v \equiv \tfrac{1}{2}\left(A_v-A_v^T\right)=\frac{1}{2}\begin{pmatrix}0&-\omega\\\omega&0\end{pmatrix}.
$$

(2.28)

Thus, the local vorticity rotates the wavefront normal. Alternatively, we can deduce this effect by reformulating (2.26) as $\mathrm{d}\phi_i/\mathrm{d}t=\epsilon_{ijk}\omega_j\phi_k-\phi_j(\partial u_i/\partial x_j)$ for an isothermal case (cf. Whitham 1974; Pierce 1989). As seen later (figures 11–13), when the local

vorticity is sufficiently strong, ray trajectories create loops and total internal reflection occurs. By contrast, if the local vorticity is weak, as would occur near the saddle points, the effect of refraction diminishes and rays tend to penetrate the mixing layer. Thus, the rotation term plays an important role in the shock-leakage mechanism. Note that the shear-strain term S_v also contributes to the rotation at a comparable level, and its effect has a similar trend as R_v, as discussed in §4.2.

Knowing the contribution from the velocity gradient tensor A_v, consider the effects of temperature gradient. The steady part of the temperature effect has been discussed in the previous section. Hence, the focus in this section is on the unsteady part of temperature effects, which may be categorized into two parts: the compressible and entropic effects. The compressible effect refers to the contribution of temperature variation induced by a finite Mach number flow field, whereas the entropic effect refers to the contribution due to the deformation of the temperature field mainly associated with the entrainment of the mixing layer. These two effects are considered below.

First, consider the compressible effect based on the case in which the temperature ratio of the mixing layer is unity (called 'iso-thermal jet' here). Meiron, Moore & Pullin (2000) studied compressible saturated vortices in a two-dimensional mixing layer based on the Stuart vortex model (Stuart 1967). They showed that the temperature variation due to the compressible effect becomes secondary as long as $((M_1 - M_c)/2)^2$ is sufficiently small.

To quantitatively evaluate the compressible effect, we can decompose the transfer matrix A_t in (2.26) into three parts in a similar manner to the derivation of A_v. Consequently, the rotation term yields

$$R_t \equiv \tfrac{1}{2}\left(A_t - A_t^T\right) = \frac{1}{2}\begin{pmatrix} 0 & -\varpi \\ \varpi & 0 \end{pmatrix}, \tag{2.29}$$

where

$$\varpi \equiv \frac{1}{2a^2}\left(u\frac{\partial a^2}{\partial y} - v\frac{\partial a^2}{\partial x}\right). \tag{2.30}$$

This scalar, ϖ, gives the extra rotation effect on the wavenumber vector due to temperature variation. In fact, numerical results shown later confirm $|\varpi| \ll |\omega|$. The rate of rotation due to the shear-strain term S_t becomes equivalently small.

For non-isothermal jets, the entropic effect becomes appreciable. The entropy variation via R_t and S_t in a hot jet alleviates the rotation effect, while that in a cold jet enhances it. Thus, this effect follows the trend derived in the steady mixing-layer analysis in which rays should more easily penetrate the mixing layer and propagate more toward downstream for a hot jet.

Finally, consider the inhomogeneous term B in (2.26) by comparing the steady and unsteady cases. If the mixing layer is steady, only the y-component exists in B and the result of the steady analysis is valid regardless of the thickness of the mixing layer. Now, the temperature contour (for example, Case A in figure 6) indicates that the unsteady temperature field near the saddle point may be locally approximated by simply rotating the steady field by an angle $-\alpha$. Thus, the difference of B between the steady and unsteady cases is given by

$$B^{un} - B^{st} = \left(\frac{1}{2a^2}\frac{\partial a^2}{\partial y}\right)^{st}\begin{pmatrix} -\sin\alpha \\ 1 - \cos\alpha \end{pmatrix} \quad \text{as} \quad \alpha \to 0, \tag{2.31}$$

where 'st' and 'un' stand for steady and unsteady cases, respectively. With a reasonable value of α, say $0 < \alpha < \pi/4$, the orientation of the vector in (2.31) $(-\sin\alpha, 1-\cos\alpha)^T$
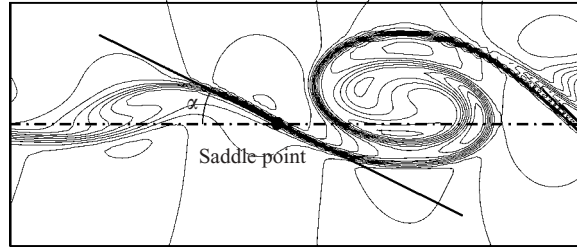
FIGURE 6. Slope of the temperature contour. The definition of α is shown. The temperature contour is taken from Case A (see table 2).

Δt	N_x	N_y	Δx	Δy	$X_{in}, X_{exit}, X_{max}$	$Y_{min}, Y_{bottom}, Y_{top}, Y_{max}$
1/96	1200	450	$0.03 \sim 0.17$	$0.04 \sim 0.12$	$5.00, 54.71, 83.00$	$-11.62, -8.62, 17.00, 20.00$

TABLE 1. Parameters for computation in DNS. Δt denotes the time step ($\times \delta_V / a_2$). N_x and N_y represent the numbers of grid points in the x- and y-directions, respectively. Likewise, Δx and Δy denote the grid sizes in the physical domain in those directions. The length scale was normalized by the vorticity thickness δ_V defined by (3.1). See figure 7 for a diagram of the computational domain. The grid is stretched in the x-direction in the buffer zone.

Case	T_1/T_2	$Re_1 \equiv \rho_1 u_1 \delta_V / \mu_1$	$Re_2 \equiv \rho_2 a_2 \delta_V / \mu_2$	ω	$\mathrm{Re}[k_x]$	$\mathrm{Im}[k_x]$
A	0.75	3000	1721	0.3927	0.6166	−0.2603
B	1.0	2000	1667	0.3927	0.5795	−0.2656
C	1.5	1200	1648	0.3927	0.5310	−0.2763

TABLE 2. Parameters of flow fields in DNS. ω, $\mathrm{Re}[k_x]$, and $\mathrm{Im}[k_x]$ denote the angular frequency, the real part of the wavenumber, and that of the imaginary part for the instability waves, respectively.

lies in the same quadrant as or opposite quadrant to (the second or fourth) the normal to the shock-front $(\phi_x, \phi_y)^T$ for leaking rays. Recall that the direction normal to the shock-front evolves over the angle range of $\theta_1 \sim [\arccos(-1/M_1), \pi)$ as it propagates across the mixing layer. Therefore, the term B mainly contributes to expansion or compression of the wavenumber vector, but barely to rotation of the shock-front.

These qualitative analyses regarding the rotation effect from each term are verified using DNS in § 4.2.

3. Numerical procedures

3.1. *Direct numerical simulation (DNS)*

In this study, the full Navier–Stokes equations were explicitly solved in two-dimensions. For time marching, the fourth-order Runge–Kutta scheme was used, and the time step was set to be constant. For spatial derivatives, the sixth-order Padé scheme was used at interior points. For the boundary points, lower order (third and fourth) Padé schemes were used (see Lele 1992 for details). The time step, the grid size, the domain size, etc. are specified in table 1.

To investigate the temperature effects of the mixing layer, three different temperature ratios were simulated (see table 2). The initial velocity field was found by solving compressible boundary-layer equations with the boundary conditions being
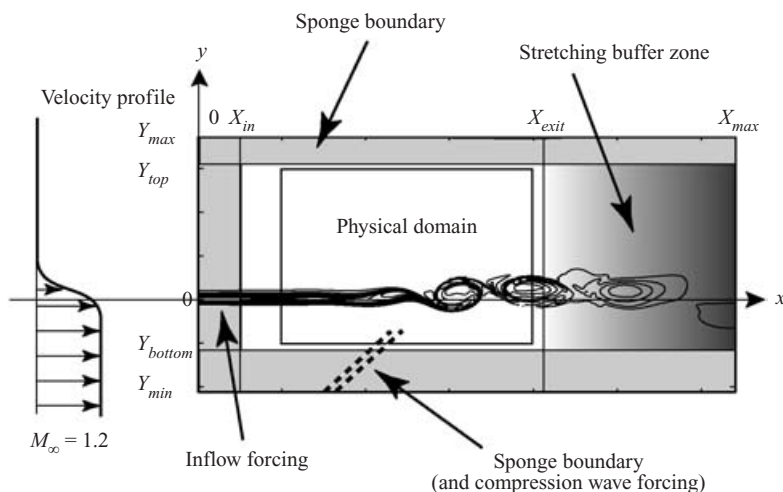
FIGURE 7. The computational domain for DNS.

$M_1 = 1.2$, $p_1 = 1$ and $T_1 = 1$ at $y = -\infty$, and $M_2 = 0$ and $p_2 = 1$ at $y = \infty$. T_2 and Reynolds numbers are specified in table 2. The initial temperature field was given by the Crocco–Busemann relation. The Prandtl number was set to be $Pr = 0.7$. The Reynolds numbers were selected so that the viscous effects in the ambient region were similar in all cases (see Re_2 in table 2). In computation, all quantities are normalized by the vorticity thickness δ_V and the ambient speed of sound $a_\infty (= a_2)$. The vorticity thickness is defined as

$$\delta_V = \frac{U_x}{(\partial U_x/\partial y)_{max}} \tag{3.1}$$

at $x = 20\delta_V$, where the velocity profile was set so that $\partial U_x/\partial y$ takes maximum at $y = 0$.

For the boundary treatment, the non-reflecting boundary conditions (Giles 1990) were used. In addition, so-called 'damping-sponges' (Freund 1997) were implemented at the inflow, the top, and the bottom regions (see figure 7) to prevent spurious reflection of acoustic waves. In the exit zone, the grid spacing was stretched (stretching ratio was $\Delta x_{i+1}/\Delta x_i = 1.04$), and the 'supersonic convection terms' (Freund 1997) as well as the following low-pass explicit filter (Colonius, Lele & Moin 1993) were applied in the flow direction (see Lui & Lele 2001 for details):

$$\hat{f}_n \equiv a(x)f_n - \tfrac{2}{3}[a(x)-1](f_{n+1}+f_{n-1}) + \tfrac{1}{6}[a(x)-1](f_{n+2}+f_{n-2}), \tag{3.2}$$

where

$$a(x) = \tfrac{5}{8} + \tfrac{3}{8} \times \frac{1}{1+e^{-c(x-x_t)/(x_p-x_t)}}. \tag{3.3}$$

The parameters shown above were set to be $c = 3$, $x_p = 53\delta_V$, and $x_t = 58\delta_V$; thus, there is no filtering in the physical domain with the filter coefficients being gradually activated toward the exit buffer zone. Additional details and validation tests can be found in Suzuki (2001).

Through the inflow sponge, Kelvin–Helmholtz instability waves were forced at a single frequency of $f^{IN} = 1/16$, which is slightly lower than the most unstable eigenmode to avoid vortex pairings in the domain of interest. The dispersion relation for spatial instability waves is shown in figure 8. The eigenfunctions were calculated
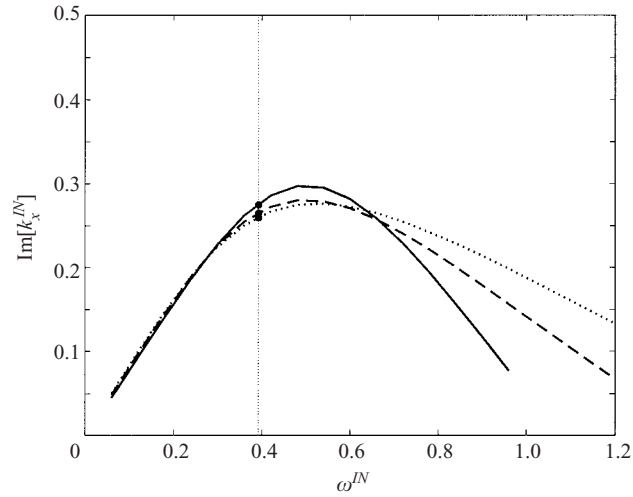
FIGURE 8. Growth rate of instability waves. Dispersion relations were calculated based on the initial velocity profile of DNS ($M_1 = 1.2$) at $x = 5\delta_V$: $\cdots$, cold jet (Case A); $---$, iso-thermal jet (Case B); ——, hot jet (Case C). ● denotes the forcing frequency in DNS.
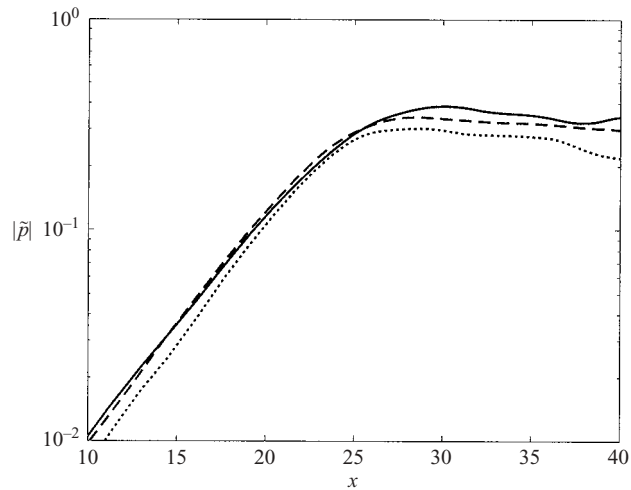

FIGURE 9. Pressure disturbance levels of instability waves. Pressure amplitudes at the centre line ($y = 0$) are plotted. Two time-periods of the instability waves were processed using discrete Fourier transform in DNS: $\cdots$, cold jet (Case A); $---$, iso-thermal jet (Case B); ——, hot jet (Case C). Note that the amplitude in Case A decreases toward downstream because the centreline of the mixing layer considerably deviated from $y = 0$.

by a shooting method. The forcing levels of the instability waves were tuned so that their pressure levels in the domain of interest became similar in all cases (see figure 9).

To avoid computational difficulties, a compression wave was imposed to simulate a shock wave. It was extended from the bottom sponge region only after vortices had developed fully ($t \gtrsim 100$), and the interaction with the unsteady vortices was computed. The position of the compression wave was set so that it would interact with the mixing layer at $(35.0, 0)$ if the mixing layer was steady. The amplitude of the compression wave in the free stream was set to be $\Delta p / p_\infty \approx 0.10$, and its width
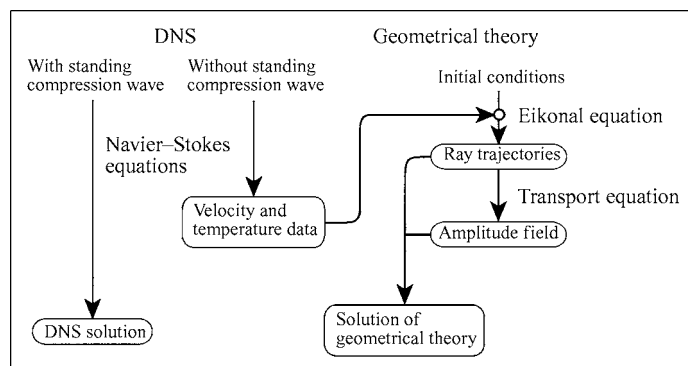
FIGURE 10. Flowchart of the numerical methods.

to be $\Delta w / \delta_V = 1.8 \cos(-\theta_1^M)$. The pressure profile of the wave was specified as a hyperbolic tangent function. Across the width of the compression wave defined above, approximately 40 grid points were included. An expansion wave of the same intensity was also imposed downstream on the bottom sponge to suppress the deflection of the mixing layer. To measure the amplitude of shock noise, 60 observer points were distributed on a circular arc using the grid points of the DNS with a radius of $R \approx 14\delta_V$ centred at $(35.0, 0)$. The pressure jumps due to the compression wave were recorded at these points. The detailed procedure to extract pressure jumps from DNS is described in the Appendix.

3.2. *Time-dependent geometrical acoustics scheme*

To study the evolution of shock-fronts, the eikonal equation was solved using the unsteady DNS base flow without a compression wave. A simple flowchart is given in figure 10. The ODE system of the eikonal equation (2.6)–(2.10) was numerically integrated using the standard fourth-order Runge–Kutta scheme with the same time step as DNS. The velocity and temperature from DNS were found from the six nearest DNS grid points using a second-order interpolation. The initial conditions for the compression wave given in (2.15)–(2.20) were imposed at the bottom sponge in figure 7, where $a_s = a_1$ and $M_s = M_1$. To calculate the threshold of the shock leakage, the initial positions of characteristic lines were $x_s \in [10.0, 35.0]$, and $y_s = -7.5$ in all cases (figures 11–13). A total of 251 rays was issued. On the other hand, to calculate shock-fronts over time, the initial positions were aligned on two lines with $\Delta w / \delta_V = \pm 0.02 \cos(-\theta_1^M)$ apart from the centreline of the compression wave: the angle normal to the compression wave is given by $\theta_1^M \equiv \arccos(-1/M_1)$. Here, 200 rays were distributed on each line. To calculate amplitude based on the Blokhintzev invariant (2.14), the area change was computed using six adjacent rays (three rays on each line). Finally, the computed amplitude directivity was fit by an eighth-order polynomial. The rays were also issued only after the vortices had developed fully $(t \gtrsim 100)$.

4. Results and discussion

4.1. *Trajectories of weak shock waves*

To investigate the threshold for shock leakage, the trajectories of shock-fronts computed based on the time-dependent eikonal equation system are shown in figures 11–13. Figure 11 (Case B) shows that shock waves tend to leak between
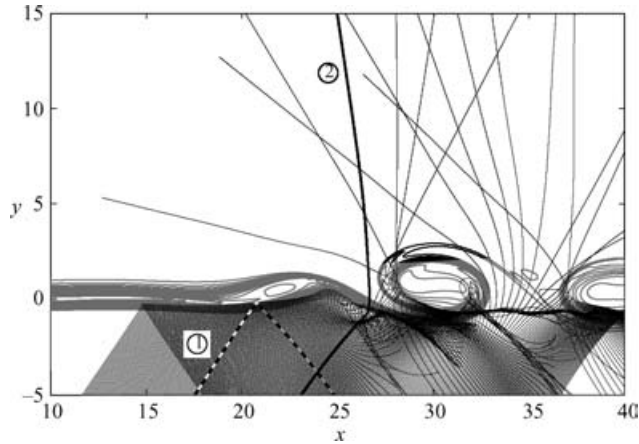
FIGURE 11. Shock-front trajectories in an iso-thermal jet mixing layer (Case B). Vorticity contour at the time when the rays with the initial conditions pass $y = 0$ is overlapped. ① and ② denote the trajectories (drawn by the thicker dashed and solid lines, respectively) discussed in figures 14 and 15.
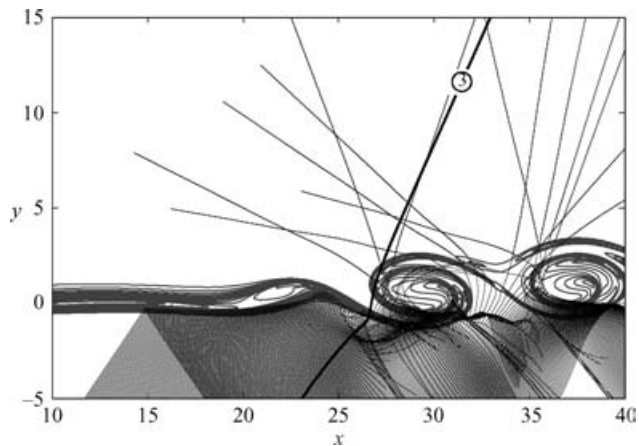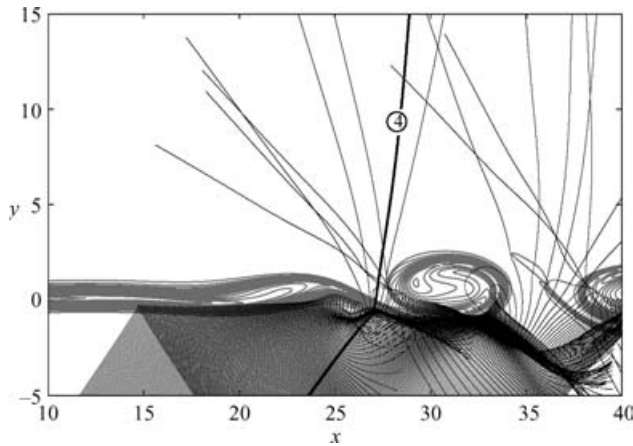

FIGURE 12. Shock-front trajectories in a cold jet mixing layer (Case A). Notation is the same as figure 11. ③ denotes the trajectory (drawn by the thicker line) discussed in figures 19 and 20.

the saddle point and the trailing edge of the vortex. As conjectured in §2.3, sound leakage occurs near the saddle point, in which local vorticity becomes weak. Moreover, as the vortices develop, the number of rays penetrating the mixing layer increases: more rays penetrate near the downstream saddle point (around $x \in (33, 37)$) than the upstream saddle point ($x \sim 28$) in figure 11.

These features of shock leakage are consistent with the DNS study of Manning & Lele (2000). They also observed that compression waves penetrate between the vortices by computing the linearized Euler equations with the Stuart vortices. Similarly, Suzuki & Lele (1999) numerically studied scattering problems in subsonic mixing layers ($M_1 = 0.3$) in two dimensions, and showed that plane waves whose angle of incidence is greater than the critical angle can leak across a subsonic vortex-laden mixing layer near saddle points.

FIGURE 13. Shock-front trajectories in a hot jet mixing layer (Case C). Notation is the same as figure 11. ④ denotes the trajectory (drawn by the thicker line) discussed in figures 19 and 20.

The series of figures 11, 12 and 13 compares the shock leakage for different temperature ratios. In these figures, an attempt was made to synchronize the relative phases of the vortices (the centre of the saddle point is about $x \approx 27$) to clearly compare these cases. As discussed in §2.2 (see figure 5), the analysis based on a steady mixing layer predicts greater leakage as the temperature of the jet increases. In fact, the comparison of these figures demonstrates that as the temperature on the high velocity side (the lower side) increases, the number of rays penetrating the first saddle point ($x \sim 27$) increases, i.e. the number of rays is 4, 6 and 8 for the temperature ratios of $T_1/T_2 = 0.75$, 1.0 and 1.5, respectively. However, when the vortices are fully developed, the spacings of the vortices become more important, and the number of rays penetrating the mixing layer do not follow the steady mixing-layer analysis. At the second (downstream) saddle point, the number of rays changes to 11, 12 and 9 for $T_1/T_2 = 0.75$, 1.0 and 1.5. Instead, the radiated direction of the leaked rays tends to lean toward downstream, as discussed later. Note that the phases of the vortices are not exactly synchronized at the second saddle point since the wavelength of the instability waves varies as the temperature ratio changes (see $\text{Re}[k_x]$ in table 2).

4.2. *Rotation effects from the base flow*

Now, the rotation effect on ray trajectories from each term is confirmed referring to the analyses in §2.3. Defining $\boldsymbol{n}_\phi \equiv (\phi_x, \phi_y)^T/|(\phi_x, \phi_y)^T|$, the rate of rotation $\dot{\theta}$ due to S_v is given by

$$\dot{\theta}(S_v) \equiv \boldsymbol{n}_\phi \times [S_v \boldsymbol{n}_\phi - (S_v \boldsymbol{n}_\phi \cdot \boldsymbol{n}_\phi)\boldsymbol{n}_\phi], \tag{4.1}$$

while the rate of rotation due to R_v is simply given by $\dot{\theta}(R_v) = \omega/2$ from (2.28). Figure 14 compares these contributions to the rotation rate for two representative rays (which can be identified in figure 11). Figure 14(a) confirms that the diminished local vorticity near the saddle point reduces the overall turning of the wavefront. Figure 14(b) shows that the shear-strain term S_v contributes to the rotation at a comparable level and even weakens the rotation effects near the saddle points: their net rotation effects are opposite for trajectories 1 and 2 because their wavefront normals are oriented on opposite sides to the principal axis of the matrix S_v as the rays approach the saddle point. For the trajectory 1, the wavefront is rotated by a total angle of 71.4° (the net area under the sum of the curves in figures 14(a) and
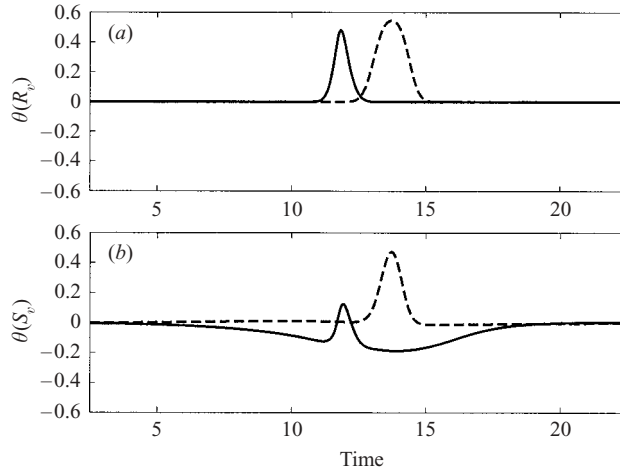
FIGURE 14. Rate of rotation from transfer matrix A_v. The rates of rotation for two rays denoted in figure 11 (Case B, isothermal) are plotted: $---$, trajectory 1; ——, trajectory 2: (a) for R_v; (b) for S_v.

Trajectory number	R_v	S_v	R_t	S_t	B
Case B, ①	43.0	28.4	0.9	1.5	4.3
Case B, ②	18.9	−60.5	−0.2	−2.0	−9.2
Case A, ③	10.5	−96.5	4.2	0.2	2.1 (26.2)
Case C, ④	26.8	−64.4	−2.7	−4.0	−37.8 (−44.5)

TABLE 3. Net rotation angle from each component. The values in parentheses in the column for B are the steady values.

14(b) excluding the temperature effect), which yields total internal reflection. On the other hand, that for the trajectory 2 is rotated by $-41.6°$ (refer to the columns for R_v and S_v in table 3); thus, this ray can penetrate the mixing layer.

Figure 15 depicts the rates of rotation due to R_t and S_t for the same trajectories as figure 14 (the definition is similar to (4.1)). It shows that the overall effect from A_t is much smaller than that from A_v for the isothermal case (see table 3 again).

Furthermore, the quantity ϖ is computed based on DNS and compared with the vorticity ω in three cases (figures 16–18). Here, the convective velocity is assumed to be $M_1 a_1/2$. Figure 17 (isothermal jet, Case B) confirms that the effect of temperature gradient is much smaller than the vorticity, i.e. $|\varpi| \ll |\omega|$. Thus, the effect of temperature gradient associated with compressibility is negligible.

Next, consider the entropic effect for the application of non-isothermal jets. Figures 16 and 18 (Cases A and C) compare the contours of ω and ϖ for cold and hot jets, respectively. They consistently show that the variations in ω and ϖ are comparable, although both become small near the saddle points. Figure 19 shows the rates of rotation due to R_t and S_t in cold and hot jets (their trajectories 3 and 4 can be identified in figures 12 and 13, respectively), and table 3 compares their net rotation angles. They show that the magnitudes of the rotation angles in the non-isothermal cases are greater than those in the isothermal case (figure 15), but relatively small. The important observation is that the entropy variation in a hot jet alleviates the
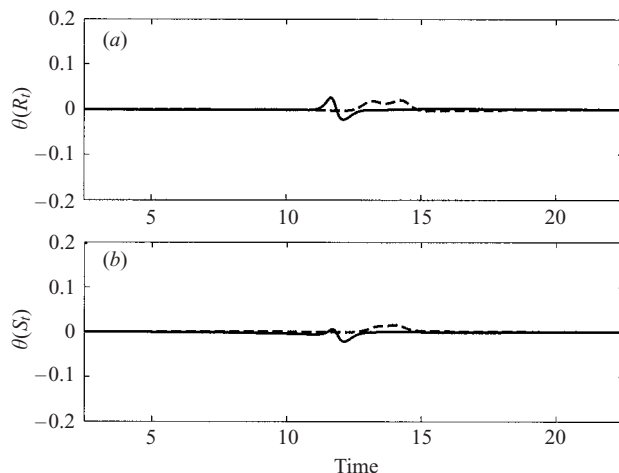
FIGURE 15. Rate of rotation from transfer matrix A_t. Notation and conditions are the same as figure 14: (*a*) for R_t; (*b*) for S_t.
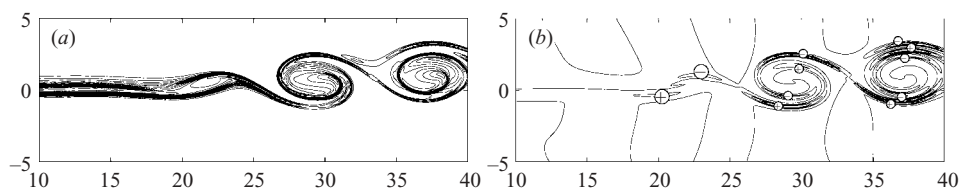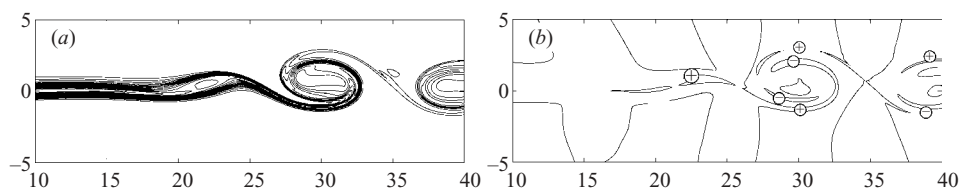

FIGURE 16. Flow quantities of an cold jet mixing layer (Case A, $M_1 = 1.2$ and $T_1/T_2 = 0.75$). (*a*) ω: vorticity contour, $\omega_{min} = 0.1$ and $\omega_{max} = 1.5$ with the interval of $\Delta\omega = 0.1$. (*b*) ϖ: contour of the rotation rate due to temperature gradient. $\varpi_{min} = -0.5$ & $\varpi_{max} = 0.4$ with the interval of $\Delta\varpi = 0.1$. $\oplus$ denotes the counterclockwise rotation, and $\ominus$ the clockwise rotation.

FIGURE 17. Flow quantities of an iso-thermal jet mixing layer (Case B, $M_1 = 1.2$ and $T_1/T_2 = 1.0$). (*a*) ω: vorticity contour, $\omega_{min} = 0.1$ and $\omega_{max} = 1.6$ with the interval of $\Delta\omega = 0.1$. (*b*) ϖ: contour of the rotation rate due to temperature gradient. $\varpi_{min} = -0.10$ and $\varpi_{max} = 0.10$ with the interval of $\Delta\varpi = 0.05$. The rest of the notation is the same as figure 16.

rotation effect, whereas that in a cold jet enhances it. It should be remembered that the same trend was observed in the steady mixing-layer analysis.

Finally, figure 20 compares the rates of rotation from B in (2.26) between the steady and unsteady cases for cold and hot jets. Note that the magnitudes of these rates are comparable to or even larger than those from A_v (refer to figure 14 and table 3). Both cold and hot jet cases show that although the effective duration of rotation becomes shorter, the net rotation angle does not change significantly (compare the
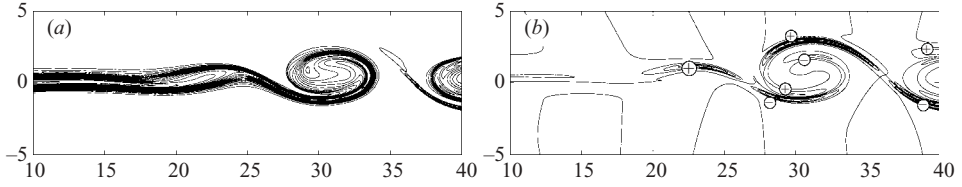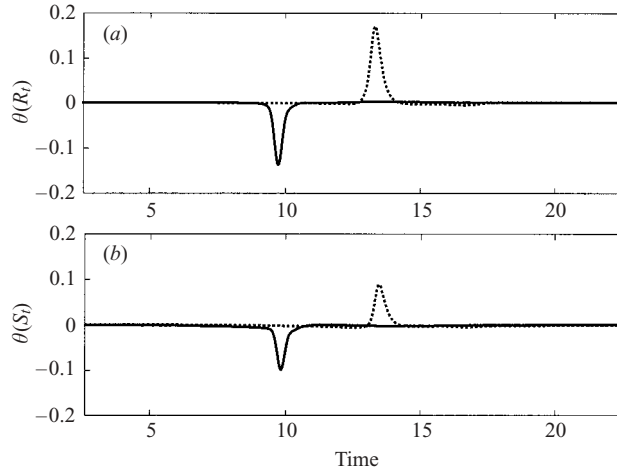
FIGURE 18. Flow quantities of a hot jet mixing layer (Case C, $M_1 = 1.2$ and $T_1/T_2 = 1.5$). (*a*) ω: vorticity contour, $\omega_{min} = 0.1$ and $\omega_{max} = 1.9$ with the interval of $\Delta\omega = 0.1$. (*b*) ϖ: contour of the rotation rate due to temperature gradient. $\varpi_{min} = -0.4$ and $\varpi_{max} = 0.8$ with the interval of $\Delta\varpi = 0.1$. The rest of the notation is the same as figure 17.

FIGURE 19. Rate of rotation from transfer matrix A_t for cold and hot jets. The rates of rotation are compared in non-isothermal cases: $\cdots$, cold jet (Case A, trajectory 3 in figure 12); and ——, hot jet (Case C, trajectory 4 in figure 13). (*a*) for R_t; (*b*) for S_t.
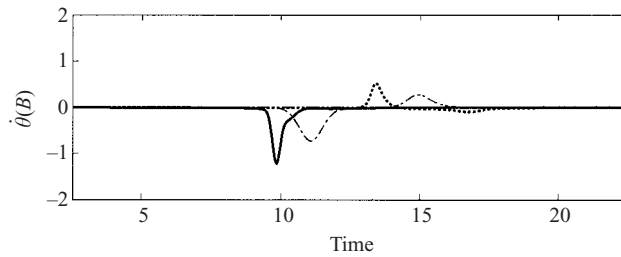
FIGURE 20. Rate of rotation from input vector B for cold and hot jets. The rates of rotation are compared in non-isothermal cases: $\cdots$, cold jet in an unsteady case (Case A, trajectory 3 in figure 12); $-\cdot\cdot-$, that in a steady case; ——, hot jet in an unsteady case (Case C, trajectory 4 in figure 13); $-\cdot-$, that in a steady case.

values in the column for B in table 3). Thus, the unsteady effect via the term B is relatively small.

4.3. *Shock-front evolution*

The time evolution of the shock-fronts from geometrical acoustics is presented in figure 21 (iso-thermal case, Case B). This figure shows that an oblique shock wave
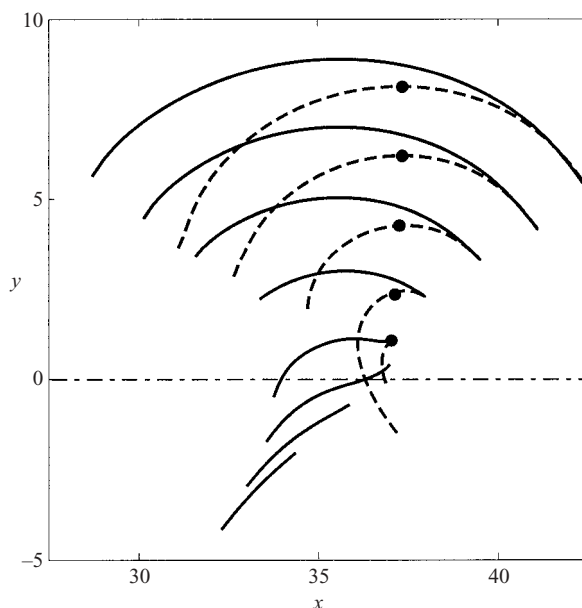
FIGURE 21. Evolution of the shock-front. Shock-fronts were solved by the eikonal equation with the base flow in Case B: ——, compression waves; − − −, expansion waves. ● keeps track of a certain point on shock-fronts. The shock-fronts are drawn every $2 \times \delta_V/a_2$.

creates a kink and forms two branches as it radiates into the far field. The wavefronts become nearly circular, and they propagate over wide angles including the upstream direction. Knowing that such a kink corresponds to the reflection point of a shock-cell, the branch propagating behind is considered to be an expansion wave. When the strength of the shock is sufficiently weak, the acoustic amplitude field can be calculated by superposing the solutions for these two branches. However, when the shock becomes nonlinear, the expansion branch is expected to spread, while the compression branch tends to maintain its total strength. This is confirmed with DNS as depicted in figure 23.

In figure 21, one point on the shock-front which initially coincides with the branch point is followed in time. This point propagates with nearly the speed of sound. This also shows that the branch point is not a characteristic line. The compression branch reflects at the branch point, and this point shifts to the expansion branch.

Figures 22 and 23 compare the evolution of shock-fronts found from the eikonal equation and from DNS. They show fairly good agreement in which the shock wave starts to leak near the saddle point and forms a compression branch followed by an expansion branch. However, the wavefronts calculated using DNS tend to propagate forward, and their shape spreads over a wider angle. Recall that in geometrical acoustics the compression wave must be weak ($\Delta p/p_\infty \to 0$), while in DNS it is finite ($\Delta p/p_\infty \sim 0.10$). Therefore, the nonlinearity of the shock wave may cause such discrepancies even though the base flow field does not change significantly.

4.4. *Temperature dependence of shock noise amplitude*

Finally, figures 24–26 compare the amplitude of compression waves between DNS and the geometrical theory for different temperature ratios. All three figures show
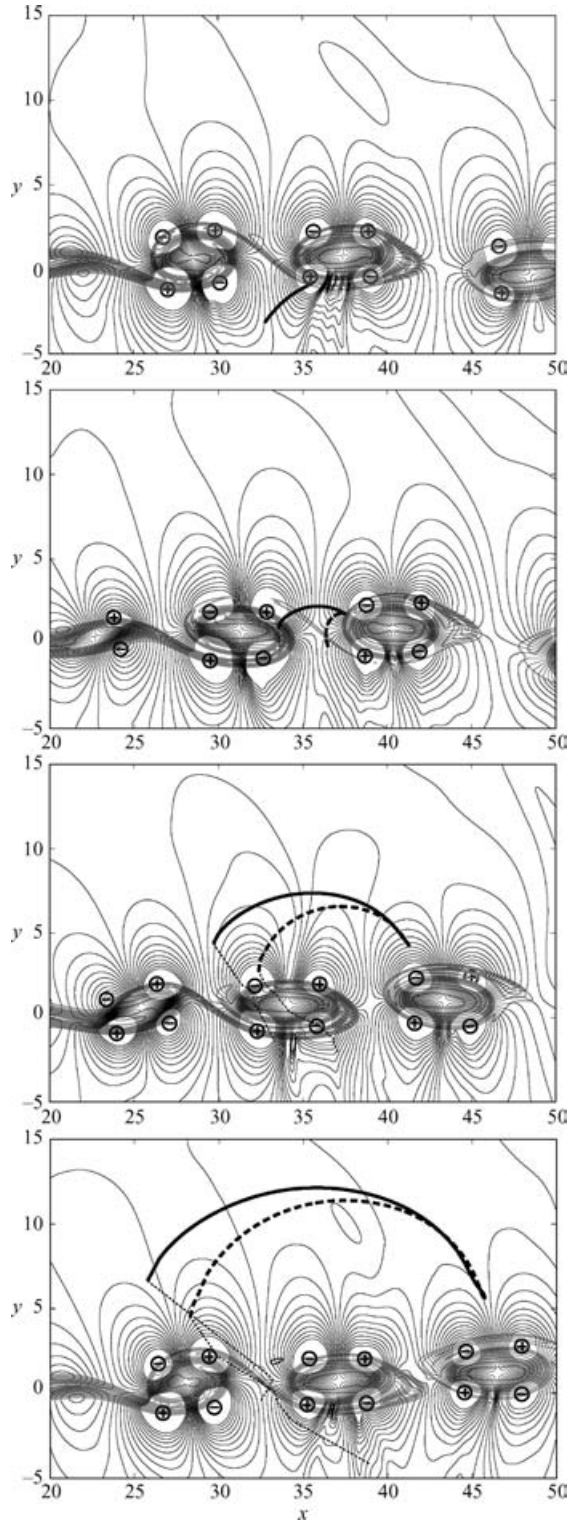
FIGURE 22. Evolution of the shock-front calculated using the eikonal equation in Case B. Shock-fronts are drawn with dilatation and vorticity contours in the course of time (interval of $\Delta t = 5$). $\oplus$ and $\ominus$ indicate expansion and compression, respectively.
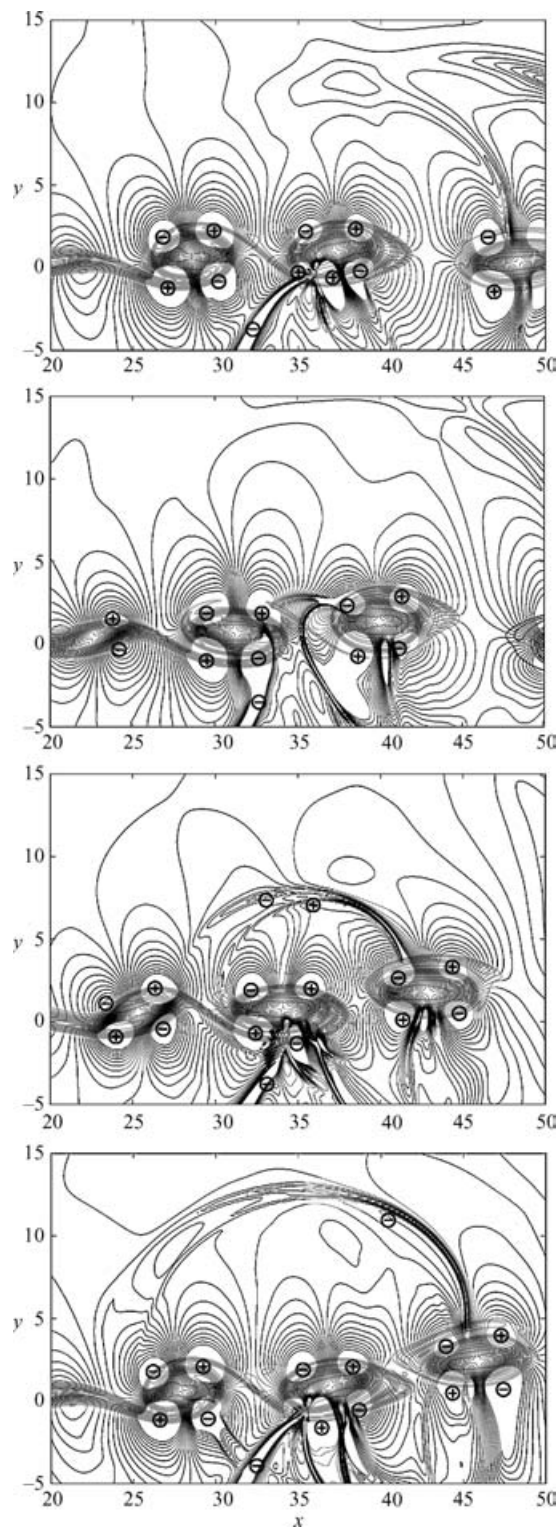
FIGURE 23. Evolution of the shock-front calculated in DNS. A compression wave is imposed, and dilatation fields corresponding to the series of figures 22 are shown. Notation and time generation are the same as figure 22.
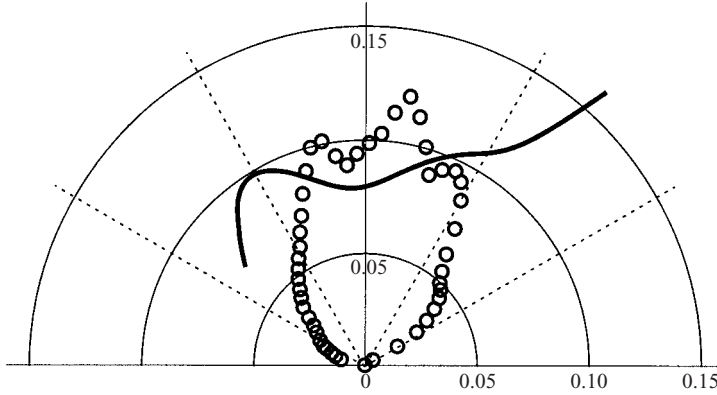
FIGURE 24. Comparison of compression wave amplitude between DNS and geometrical theory for a cold jet mixing layer (Case A). The pressure ratios of the compression wave at distance $R \approx 14\delta_V$ centred at $(35.0, 0)$ are plotted. The pressure ratio is defined as $(\Delta p_{R=14})/(\Delta p_{y_{min}})$: $\bigcirc$, DNS; ———, geometrical theory.
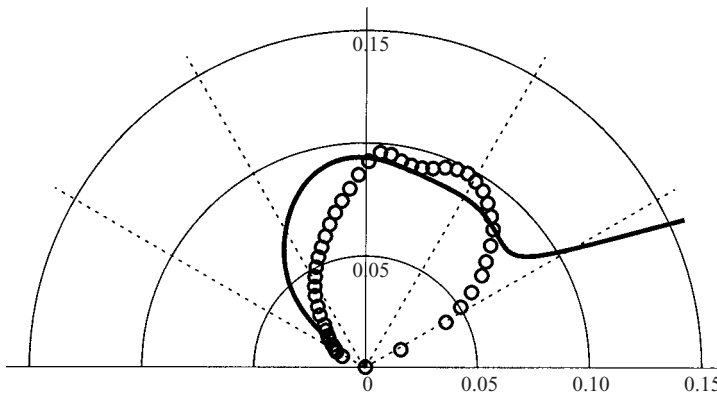

FIGURE 25. Comparison of compression wave amplitude between DNS and geometrical theory for an iso-thermal jet mixing layer (Case B). Notation is the same as figure 24.
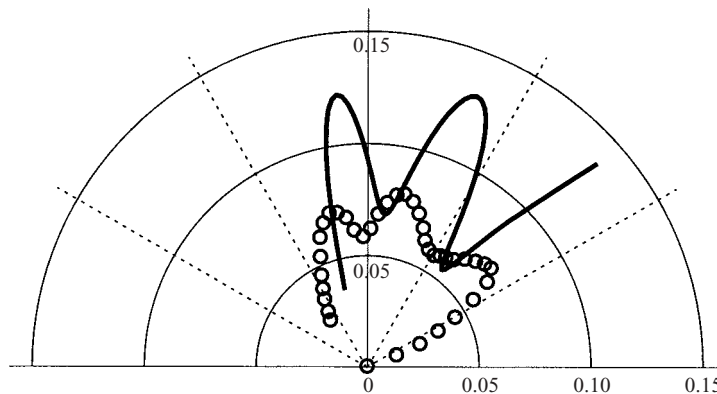

FIGURE 26. Comparison of compression wave amplitude between DNS and geometrical theory for a hot jet mixing layer (Case C). Notation is the same as figure 24.
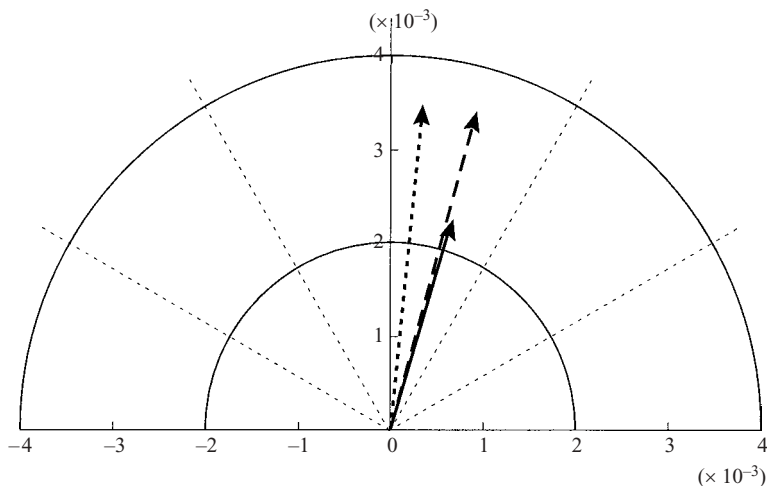
FIGURE 27. Directivity of integrated shock noise intensity at different temperature ratios. Integrated intensities defined by $(\tilde{I}_x, \tilde{I}_y) \equiv (\int_0^\pi p^2(\theta)\cos\theta \, d\theta, \int_0^\pi p^2(\theta)\sin\theta \, d\theta)$ obtained from figures 24–26 are plotted in a polar plot: $\cdots$, cold jet (Case A); $---$, iso-thermal jet (Case B); and ——, hot jet (Case C).

that the overall sound pressure level of DNS is comparable to the geometrical theory, although the detailed directivity of shock noise is not predicted well. It is interesting to note that the radiation pattern obtained from DNS in the hot jet case (figure 26) is similar to the peak tonal noise radiation pattern experimentally obtained by Walker & Thomas (1997) (their figure 6). It should be mentioned that it is very difficult to distinguish clearly the acoustic pressure from the hydrodynamic disturbances in DNS. The estimated amplitude error may be as much as $\sim \pm 15\%$ (refer to the Appendix). Moreover, the distortion of the mean flow as well as the nonlinear propagation effects can cause discrepancies, as mentioned above.

The series of figures 24, 25 and 26 indicates that the shock noise intensity is weakly enhanced toward downstream as the jet temperature is increased (see figure 27 for an integrated measure of the intensity). Recall that the analyses in §2 imply that shocks can more easily leak and propagate more toward downstream as the jet temperature increases; moreover, the spacings between the vortices becomes wider as well (refer to $\text{Re}[k_x]$ in table 2). This may explain the directivity changes. However, the total pressure amplitude seems to decrease as the jet temperature increases, which appears to contradict the analyses. As figure 9 shows, the amplitudes of the disturbance level do not perfectly coincide. In fact, the disturbance amplitude slightly increases downstream as the jet temperature increases, although the viscosity inside the jet becomes greater. Thus, a more complete parametric study is necessary to investigate the temperature dependence.

In fact, previous numerical work by Shen & Tam (2000) reported a similar trend (their figure 10). Their result also showed that the downstream intensity increases significantly as the jet temperature increases. However, the dipole-like radiation pattern which they computed is not observed in the present results. It should be emphasized that Shen & Tam (2000) computed the sound pressure levels from multiple shock noise sources in a whole round jet, while the current result represents the strength of the compression wave from a single noise source in two-dimensions.

Importantly, the radiation pattern changes considerably when the superposition of the noise from all sources is considered.

5. Conclusions

In this study, shock noise associated with a supersonic mixing layer is investigated theoretically and computationally. The key points are summarized as follows.

The mechanism of shock noise is explained using a geometrical theory which is analogous to geometrical acoustics. From the system of the eikonal equation, it is deduced that the shock tends to leak near the saddle points of vortices convected in the mixing layer. In fact, this mechanism is numerically demonstrated by solving the time-dependent eikonal equation using the unsteady DNS data.

The time evolution of the shock-fronts and the amplitude of the shock noise are calculated based on the time-dependent eikonal equation using the unsteady DNS data, and the results are in good agreement with the full DNS for the shock-fronts. Both results show that radiated shock noise forms two branches: a compression wave followed by an expansion wave. However, the comparison of amplitude does not agree quantitatively in terms of directivity. Compared with the previous theories of shock–vortex interaction, time-dependent geometrical acoustics can capture fast shock motions (i.e. the propagation speed is comparable to the speed of sound). Instead, the present theory uses the simplified condition across the shock, i.e. isentropic assumption, and neglects any hydrodynamic response from the interaction. This probably causes the discrepancy in amplitude.

The temperature dependence of shock leakage is analysed based on an analogy with total internal reflection in a steady mixing layer. The analysis suggests that shock waves leak more easily as the jet temperature increases. The numerical results from both geometrical theory and DNS also follow the trend that the direction of the radiated shock noise weakly shifts downstream as the jet temperature increases. However, detailed parametric study is necessary for definitive prediction of the shock noise amplitude.

Previous experimental studies (such as, Walker & Thomas 1997; Panda 1999) have indicated that the shock noise is most intensive somewhere between the second and fourth shock-cell locations. We can understand such a trend based on this study. Shock waves can leak through the mixing layer and generate intense noise only after the unsteady vortices have developed sufficiently. However, when smaller-scale eddies develop further downstream, the organized vortical structure is disrupted so that clear saddle points are no longer formed, and the intensity of the shock noise is reduced again. Since the width of shock waves is much thinner than any scales of vortical disturbances, shock-fronts can be easily scattered by turbulence (Lee, Lele & Moin 1993). Instead, broadband shock noise is generated.

On the contrary, it also implies that disruption of the organized large-scale structures may reduce the intensity of shock noise. This explains the mechanism of some noise suppression techniques (Norum 1983; Krothapalli, McDaniel & Baganoff 1990; Samimy *et al.* 1998). Some of these studies indicated that the streamwise vortices tend to disrupt the large-scale structure of the fundamental unstable mode. Such an observation also suggests that a slight exit modification could substantially influence the initial disturbance of the instability waves; accordingly, the amplitude of the screech noise can strongly change.

Thus, the shock leakage across an unsteady vortex-laden mixing layer is investigated in the context of the jet screech problem. This asymptotic analysis should help understand the shock noise mechanism.
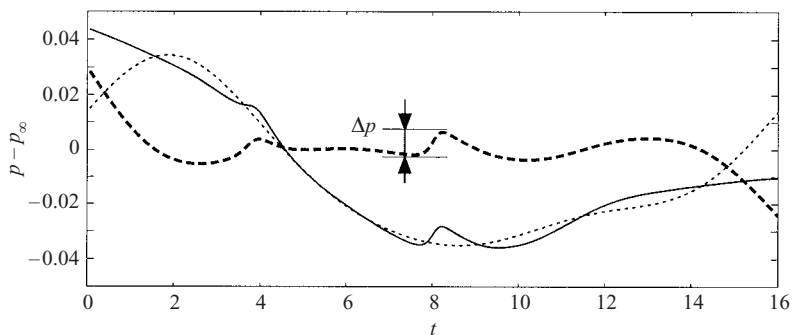
FIGURE 28. Example of extracted shock noise amplitude in DNS. Time history of pressure at $R \approx 14\delta_V$ and $\theta \approx 60°$ in Case B is plotted: ——, raw DNS data; $\cdots$, pressure profile consisting of first three modes; $- - -$, subtracted pressure profile.
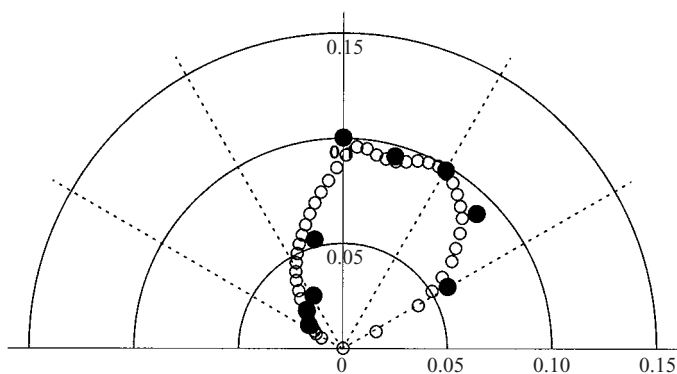

FIGURE 29. Shock noise extracted from pressure profiles and dilatation profiles. For comparison purposes, pressure jumps calculated from the dilatation profiles (denoted by ● at nine representative angles) are overlapped on those from the pressure profiles (denoted by ○) in Case B. Notation is the same as figure 24.

Appendix. Post-processing to extract shock noise amplitude

To calculate the shock noise amplitude in DNS, pressure is recorded every $\Delta t = 1/16$ at each observer position (see figure 28 for an example of a time history of pressure). However, since the hydrodynamic pressure field is still fairly large at the observer points ($R \approx 14\delta_V$), pressure jumps of shock noise cannot be measured directly in DNS. To suppress the hydrodynamic pressure, the pressure profiles were transformed into the frequency domain using a Fourier transform, and the lowest three modes were eliminated. Subsequently, they were transformed back into the time domain, and the difference between the local maximum and minimum was defined as the pressure jump Δp as shown in figure 28. In this process, the magnitude of the pressure jump is reduced approximately by 15% (base on the hyperbolic tangent

profile with the same slope); hence, this reduction was taken into account in the polar plots. To evaluate the accuracy of this data processing, dilatation profiles were similarly processed and converted to pressure jumps by integrating them in time. The comparison is shown in figure 29. The estimated error is also approximately up to 15%.

REFERENCES

BLOKHINTZEV, D. I. 1946 The propagation of sound in an inhomogeneous and moving medium. *J. Acoust. Soc. Am.* **18**, 322–328.

COLONIUS, T., LELE, S. K. & MOIN, P. 1993 Boundary conditions for direct computation of aerodynamic sound generation. *AIAA J.* **31**, 1574–1582.

FREUND, J. B. 1997 Proposed inflow/outflow boundary condition for direct computation of aerodynamic sound. *AIAA J.* **35**, 740–742.

GILES, M. B. 1990 Nonreflecting boundary conditions for Euler equation calculations. *AIAA J.* **28**, 2050–2058.

GOLDSTEIN, M. E. 1976 *Aeroacoustics.* McGraw-Hill.

HOWE, M. S. & FFOWCS WILLIAMS, J. E. 1978 On the noise generated by an imperfectly expanded supersonic jet. *Phil. Trans. R. Soc. Lond.* A **289**, 271–314.

KELLER, J. B. 1954 Geometrical acoustics. I. The theory of weak shock waves *J. Appl. Phys.* **25**, 938–947.

KERSCHEN, E. J. & CAIN, A. B. 1995 Modeling supersonic jet screech Part 2: Acoustic radiation from the shock–vortex interaction. *AIAA Paper* 95-0507.

KEVLAHAN, N. K.-R. 1996 The propagation of weak shocks in non-uniform flows. *J. Fluid Mech.* **327**, 161–197.

KROTHAPALLI, A., HSIA, Y., BAGANOFF, D. & KARAMCHETI, K. 1986 The role of screech tones in mixing of an underexpanded rectangular jet. *J. Sound Vib.* **106**, 119–143.

KROTHAPALLI, A., MCDANIEL, J. & BAGANOFF, D. 1990 Effect of slotting on the noise of an axisymmetric supersonic jet. *AIAA J.* **28**, 2136–2138.

LEE, S., LELE, S. K. & MOIN, P. 1993 Direct numerical simulation of isotropic turbulence interacting with a weak shock wave. *J. Fluid Mech.* **251**, 533–562.

LELE, S. K. 1992 Compact finite difference schemes with spectral-like resolution. *J. Comput. Phys.* **103**, 16–42.

LIGHTHILL, M. J. 1956 Viscosity in waves of finite amplitude. In *Surveys in Mechanics* (ed. G. K. Batchelor & R. M. Davies), pp. 250–351. Cambridge University Press.

LILLEY, G. M. 1974 On the noise from jet. *AGARD Conf. Proc.* 131, 1–12.

LUI, C. & LELE, S. K. 2001 Direct numerical simulation of spatially developing, compressible, turbulent mixing layers. *AIAA Paper* 2001-0291.

MANNING, T. A. & LELE, S. K. 2000 A numerical investigation of sound generation in supersonic jet screech. *AIAA Paper* 2000-2081.

MEIRON, D. I., MOORE, D. W. & PULLIN, D. I. 2000 On steady compressible flows with compact vorticity; the compressible Stuart vortex. *J. Fluid Mech.* **409**, 29–49.

MONICA, A. & PRASAD, P. 2001 Propagation of a curved weak shock. *J. Fluid Mech.* **434**, 119–151.

MOORE, F. K. 1953 Unsteady oblique interaction of a shock wave with a plane disturbance. *NACA TN-2879.*

NORUM, T. D. 1983 Screech suppression in supersonic jets. *AIAA J.* **21**, 235–240.

NORUM, T. D. 1991 Supersonic rectangular jet impingement noise experiments. *AIAA J.* **29**, 1051–1057.

PANDA, J. 1998 Shock oscillation in underexpanded screeching jets. *J. Fluid Mech.* **363**, 173–198.

PANDA, J. 1999 An experimental investigation of screech noise generation. *J. Fluid Mech.* **378**, 71–96.

PIERCE, A. D. 1989 *Acoustics: An Introduction to Its Physical Principles and Applications.* The Acoustical Society of America.

POWELL, A. 1953 On the mechanism of choked jet noise. *Proc. Phys. Soc. Lond.* B **66**, 1039–1056.

PRIDMORE-BROWN, D. C. 1958 Sound propagation in a fluid flowing through an attenuating duct. *J. Fluid Mech.* **4**, 393–406.

RAMAN, G. 1999 Supersonic jet screech: half-century from Powell to the present. *J. Sound Vib.* **225**, 543–571.

RIBNER, H. S. 1954 Convection of a pattern of vorticity through a shock wave. *NACA TN*-2864.

SAMIMY, M., KIM, J.-H., CLANCY, P. S. & MARTENS, S. 1998 Passive control of supersonic rectangular jets via nozzle trailing-edge modifications. *AIAA J.* **36**, 1230–1239.

SHEN, H. & TAM, C. K. W. 2000 Effects of jet temperature and nozzle-lip thickness on screech tone. *AIAA J.* **38**, 762–767.

STUART, J. T. 1967 On finite amplitude oscillations in laminar mixing layers. *J. Fluid Mech.* **29**, 417–440.

SUZUKI, T. 2001 Acoustic wave propagation in transversely sheared flows. PhD thesis, Stanford University, Stanford.

SUZUKI, T. & LELE, S. K. 1999 Acoustic scattering from a mixing layer: role of instability waves. *AIAA Paper* 99-0228.

TAM, C. K. W. 1988 The shock-cell structures and screech tone frequencies of rectangular and non-axisymmetric supersonic jets. *J. Sound Vib.* **121**, 135–147.

TAM, C. K. W., SEINER, J. M. & YU, J. C. 1986 Proposed relationship between broadband shock associated noise and screech tones. *J. Sound Vib.* **110**, 309–321.

TAM, C. K. W. & TANNA, H. K. 1982 Shock associated noise of supersonic jets from convergent-divergent nozzles. *J. Sound Vib.* **81**, 337–358.

WALKER, S. H. & THOMAS, F. O. 1997 Experiments characterizing nonlinear shear layer dynamics in a supersonic rectangular jet undergoing screech. *Phys. Fluids* **9**, 2562–2579.

WHITHAM, G. B. 1974 *Linear and Nonlinear Waves in Pure and Applied Mathematics.* Wiley-Interscience.